HHS Public Access

Author manuscript

IEEE Robot Autom Lett. Author manuscript; available in PMC 2024 September 01.

Published in final edited form as:

IEEE Robot Autom Lett. 2023 September ; 8(9): 5345–5352. doi:10.1109/lra.2023.3286125.

Model-based Design of the COAST Guidewire Robot for Large Deflection

Yash Chitalia[*,1], **Achraj Sarma**[*,2], **Timothy A. Brumfiel**[3], **Nancy J. Deaton**[3], **Maxina Sheft**[4], **Jaydev P. Desai**[3],

Fellow IEEE

[1]Healthcare Robotics and Telesurgery (HeaRT) Laboratory, Department of Mechanical Engineering, University of Louisville, KY, USA. He contributed to the work presented in this paper when he was a graduate student in the RoboMed Laboratory at the Georgia Institute of Technology, GA, USA.

[2]contributed to the work presented in this paper when he was a graduate student in the RoboMed Laboratory at the Georgia Institute of Technology, GA, USA.

[3]Medical Robotics and Automation (RoboMed) Laboratory, Wallace H. Coulter Department of Biomedical Engineering, Georgia Institute of Technology, Atlanta, GA, USA.

[4]contributed to the work presented in this paper when she was an undergraduate student at the Georgia Institute of Technology.

Abstract

Minimally invasive endovascular procedures involve the manual placement of a guidewire, which is made difficult by vascular tortuosity and the lack of precise tip control. Steerable guidewire systems have been developed with tendon-driven, magnetic, and concentric tube actuation strategies to enable precise tip control, however, selecting machining parameters for such robots does not have a strict procedure. In this paper, we develop a systematic design procedure for selecting the tube pairs of the COaxially Aligned STeerable (COAST) guidewire robot. This includes the introduction of a mechanical model that accounts for micromachining-induced pre-curvatures with the goal of determining design parameters that reduce combined distal tip pre-curvature and minimize abrupt changes in actuated tip position for the COAST guidewire robot through selection of the best flexural rigidity between the tube pairs. We present adjustments in the kinematics modeling of COAST robot tip bending motion, and use these to characterize the bending behavior of the COAST robot for varying geometries of the micromachined tubes, with an average RMSE value for the tip position error of 0.816 mm in the validation study.

Index Terms—

Tendon/Wire Mechanism; Compliant Joints; Mechanisms

tbrumfiel4@gatech.edu .

*Yash Chitalia and Achraj Sarma contributed equally to this work

1. Introduction

Cardiovascular diseases (CVDs) are a group of disorders of the heart and blood vessels that can lead to heart attack, heart failure, cardiomyopathy, and peripheral vascular disease, accounting for an estimated 17.8 million deaths in 2017 [1]. The prevalence of peripheral vascular disease (PVD), in particular, has increased globally by 34.4% between 2005 and 2015 [2], resulting in approximately 60,000 deaths in the USA in 2015 [3]. PVD is caused due to lesions formed in the vascular structures at the extremities of the patients' bodies, such as calcification in the arteries at the lower legs and feet i.e., Lower Extremity Arterial Disease (LEAD). Endovascular treatment for critical limb ischemia, a form of PVD, has increased from 5.1% to 11.0% from 2003–2011 in the USA, contributing to lower hospital stays, lower mortality, and lower risk of limb amputation [3]. Manual navigation of a long and thin wire (called a guidewire) to the target lesion is often the first step in the endovascular treatment of PVDs. Guidewires typically range in diameters from 0.3556 mm–0.889 mm and in lengths from 500 mm–2600 mm.

Several actuation strategies are used to add steerability to guidewires and catheters, namely, magnetic [4], [5], electrical [6], thermal [7], hydraulic-chamber based, and mechanical (typically associated with cable-driven or concentric tube-based (CTR) robots) [8]–[10]. Traditionally cable-driven mechanisms cannot perform follow-the-leader (FTL) motion at small diameters, which is critical for traversing vascular structures [11], [12]. However, our previous work [13], we proposed a novel COaxially Aligned STeerable (COAST) guidewire robot capable of performing FTL motion in a single degree-of-freedom (2D workspace) with an outer diameter (OD) of 0.4 mm and total usable length of ~137 mm. The work presented in this paper is in most part presented in [14].

The authors in [15] present an analysis and design criteria for asymetric tendon placement in continuum manipulators, but the design procedure focuses on kinematic goals, achieved through tendon routing. The work in [16] provides design guidelines for the least complicated concentric tube robot for a given trajectory. In [17], the authors outline the geometrical constraints of the guidewire workspace which can inform the geometric optimization of the bending segments of a robotic guidewire. For discrete linkage robots, individual bending joint angle design parameters have been optimized for a given trajectory as in [18]. However, to the best of our knowledge, for notched tendon-driven guidewire robots, there is no design procedure for determining machining parameters based on desired characteristics of the manipulator. To address this, a design procedure is developed for the COAST guidewire robot to determine machining parameters based on desired combined tube precurvature and the flexural rigidity ratio between the tubes to reduce abrupt changes in the guidewire shape, commonly refered to as "snapping" motion. The contributions of this work are:

- We present a systematic approach to find the best tube pair for the COAST guidewire robot which uses a large deflection beam-bending model (derived in this work) and analysis of the coaxial-tube assembly for different notch depths to achieve the desired moderate flexural rigidity, and desired low total combined pre-curvature.

- We propose and validate a modified bending joint kinematics and statics model for the COAST robot that accounts for friction interactions of the tendon within the guidewire and the actuation mechanism.

This paper is organized as follows: We first present the mechanical designs in Section II for the COAST guidewire robot (Section II–A) and the compact actuation mechanism (Section II–B). Section III details the mechanical models developed for different aspects of the COAST guidewire; a large deflection curved beam bending model for the notched tubes (Section III–A) and curvature-stiffness modeling for coaxially combined notched tubes (Section III–B) are derived for design selection of the robot prototype, followed by a frictionbased kinematics and statics model for the actuated robot that relates curvature to required tendon stroke (Section III–C). In Section IV, we validate each of the models developed in the previous section and present the results for the large deflection beam model (Section IV–A), the combined tube curvature model (Section IV–B), and the bending joint model (Section IV–C). Finally, we present our conclusions and outline future work in Section V.

II. Mechanical Design

In this section, we briefly summarize the COAST guidewire robot introduced in [13], followed by the compact actuation system (CAS) for controlling the individual degrees-of-freedom (DoFs) of the robot.

A. COAST Guidewire

The COaxially Aligned STeerable (COAST) guidewire robot features a four-layered structure consisting of an outer, middle, and inner tube, as well as a single tendon assembled in a co-axially aligned manner (see Fig. 1(a)). The outer and middle tubes are micromachined to have a unidirectional asymmetric notch pattern [19], [20]. The middle tube is assembled within the outer tube so that the outer tube pattern is oriented at 180° with respect to the middle tube pattern to prevent mechanical interference during bending. The inner tube located within the middle tube has higher stiffness than the middle and outer tubes and is not micromachined for added stiffness. A single tendon is passed through the inner tube and terminated along the inner wall of the middle tube. The guidewire structure can therefore be divided into two segments based on the location of the inner tube:

a. A ‘Bending Segment’ (consisting only of the middle and outer tubes and the tendon), and

b. a ‘Non-bending Segment’ (consisting of all three tubes and tendon).

The inner tube’s distal end location controls the bending segment length of the robot (see Fig. 1(a)), while tendon stroke controls the bending segment joint angle. In addition, the outer tube itself can further be independently and individually advanced over the middle tube. The outer and inner tubes and the tendon are connected to three linear motors on the actuator stage, while the middle tube is fixed to the actuator stage itself. This tube is displaced when the actuator stage is advanced, retracted, or rolled. Therefore, we have five controllable variables in the system (see Fig. 2):

$$\begin{bmatrix} \psi \\ X_1 \\ X_2 \\ X_3 \\ X_4 \end{bmatrix} = \begin{bmatrix} \text{CAS Roll Angle} \\ \text{Tendon Stroke} \\ \text{Bending Segment Length} \\ \text{Outer Tube Stroke} \\ \text{Stage Feed Displacement} \end{bmatrix}$$

Actuating the above control variables allows two modes of motion (both have been demonstrated in our prior work [13]):

- Follow-the-leader (FTL) motion, achieved by actuating X_1, X_2 and X_4 simultaneously in any bending plane determined by roll angle ψ.
- Extended-feed (ExF) motion, achieved by advancing only the outer tube, X_3, thus displacing the distal tip of the robot while maintaining the current shape along the bending segment and the body of the robot.

If a location in the workspace of the guidewire robot is not reachable using FTL motion at a certain anatomical bifurcation, ExF motion may be used to advance the distal tip of the robot while retaining curvature at the bifurcation. ExF motion may also be used to retain entry in a certain vascular branch while the remaining of the guidewire components are advanced to proceed with further navigation.

The outer and middle tubes are micromachined using a femtosecond laser (WS-Flex Ultra-Short Pulse Laser Workstation, Optec, Frameries, Belgium) from stock tubes of superelastic nitinol (Edgetech Industries LLC, FL, USA; Young's modulus, $E = 40\text{~}45\,\text{GPa}$). The inner tube is made from AISI 304 stainless steel due to its added stiffness ($E_{\text{inner}} = 200\,\text{GPa}$). The tendon is a superelastic nitinol tendon with an elastic modulus of 53.965 GPa (derived experimentally in [13]). Notch parameters on both tubes (specifically notch depth, d, and lengths of the notched sections) were selected to ensure that the guidewire can traverse angles typically found in adult aortic bifurcations, e.g., branch angle within aortic bifurcation = $35^\circ \pm 11.1^\circ$ found in [21] (however, the actual angle of bending taken with respect to one of the common iliac arteries would be $180^\circ - 35^\circ \approx 145^\circ$). High accuracy measurements for notch depth, d, notch spacing, c, and notch width, h, are performed using the focusing lens in the femtosecond laser. These notch parameters are illustrated in Fig. 1(b). The relevant tube dimensions and parameters are indicated in Table I.

B. Compact Actuation System (CAS)

The COAST guidewire involves the translation of multiple tubes along with tendon actuation, each of which requires linear actuation simultaneously for performing FTL motion. The tubes and the tendon are attached within a compact actuation system (CAS), which is a cylindrical structure (see Fig. 2(a)) of length 165.11 mm and diameter 41 mm. The CAS is fixed onto the actuator stage, which is advanced/retracted using a DC Motor (Pololu Robotics and Electronics, NV, USA) attached to a lead-screw (OD: 3/8", pitch: 40 rev/in) and linear-bearing rails (indicated by X_4 in Fig. 2(a)). Rolling motion, ψ, is achieved with a DC motor (Maxon Precision Motors, MA, USA) and spur gear assembly. The cylindrical case is attached to the larger spur gear at one end, and rests on two ball

bearings at either end of the case. An exploded view of the actuator assembly is shown in Fig. 2(a)(inset). The outer and inner tubes and the tendon are actuated by DC motors (Maxon Precision Motors, MA, USA) with a lead screw assembly, while the middle tube is attached to an intermediate disk and is rigidly connected to the actuator stage itself. In each case, the lead-screws are supported on either end by locating and non-locating bearings to account for radial and axial misalignment. The attachment points for all the tubes and the tendon, as well as the control variables for the tubes ($X_1 - X_3$), are indicated in Fig. 2(b). The tendon is routed using two pulleys (see Fig. 2(a)(inset) and 2(b)) to reverse the direction of the tendon stroke (wrapping angle for the routing assembly is $\alpha = \pi$. An image of the CAS is shown in Fig. 2(c).

III. Mechanical Models

The unidirectional asymmetric notch pattern micromachining on each nitinol tube of the COAST mechanism results in a machining-induced pre-curvature due to the asymmetric heating induced deformation of the tube bodies. When the notched middle and outer tubes with these pre-curvatures are assembled (as discussed in Section II–A), the pair results in a non-zero combined pre-curvature. In addition to a desired flexural rigidity, a pair of tubes that results in the lowest combined pre-curvature (ideally, no combined pre-curvature) is desired so that the unactuated robot tip is straight and bends only when the tendon is actuated. We consider four outer tubes and three middle tubes machined with varying notch depths (shown in Table II), and model the gravity-induced deflection of the individual tubes, followed by a combined tube model to identify the tube pair with least combined pre-curvature.

A. Large Deflection Curved Beam Bending

The direction of the pre-curvature of the notched tubes corresponds to the direction of the notch pattern in the bending plane and its magnitude is a function of the depth of the rectangular notches, d (see Fig. 3(a)). We assume that in the absence of any external loading (including gravity effects), this curvature is constant across the entire length of the beam and is indicated by $\kappa_o(d) = 1/R_o(d)$ (where $R_o(d)$ is the radius of pre-curvature). This is a reasonable assumption, since the machining parameters stay constant throughout the length of the tube, and hence, pre-curvatures are distributed equally along this length (the notch depth d is dropped from the terms $\kappa_o(d)$ and $R_o(d)$ in the remainder of this section for brevity).

Therefore, individual tubes in the COAST mechanism behave like pre-curved slender cantilever beams of length L under gravity loading (see Initial Configurations, indicated by the black-colored beams in Fig. 3). Gravity induced loading results in a non-trivial deformation of these pre-curved beams (see Final Configurations, indicated by red-colored beams in Fig. 3) and this deformation is highly dependent on the initial configuration of the cantilever beam. This loading may be assumed as a distributed load, $w(s)$, which is a function of the path variable, s, with a fixed direction (along the negative y–axis in Fig. 3(a)–(b)) which is a piecewise function of the path of this pre-curved cantilever beam:

$$w(s) = \begin{cases} w_1 & s \in ((n-1)(h+c), nh+(n-1)c] \\ w_2 & \text{otherwise} \end{cases} \tag{1}$$

where, $w_1 = \pi\rho g\left(r_o^2 - r_i^2\right)$ and $w_2 = \rho g\left(r_o^2 - r_i^2\right)\cos^{-1}\left(\frac{d-r_o}{r_o}\right)$ (see Fig. 3(insets)). Here, $\rho = 6450\,\text{kg/m}^3$ is the density of nitinol, $g = 9.81\,\text{m/s}^2$, $d \geq r_o$ is the depth of the rectangular notches, c is width of each notch, h is the separation between two notched sections and $n = 1,2,\ldots,N$, is a variable representing the notch number. The notch parameters, $\{d, c, h\}$, are assumed to be uniform throughout the length of the notched sections of the tubes. Similarly, the second moment of area $I(s)$, which is also a function of the path variable, s, can be defined as follows:

$$I(s) = \begin{cases} \frac{\pi}{4}\left(r_o^4 - r_i^4\right) & s \in ((n-1)(h+c), nh+(n-1)c] \\ \left(r_o^4 - r_i^4\right)\frac{(\phi+\sin\phi)}{8} - \frac{8\sin^2\left(\frac{\phi}{2}\right)\left(r_o^3 - r_i^3\right)^2}{9\phi\left(r_o^2 - r_i^2\right)} & \text{otherwise} \end{cases} \tag{2}$$

where, $\phi = 2\arccos\left(\frac{d-r_o}{r_o}\right)$. The beam deformation equation in Cartesian coordinates for large deflections of a pre-curved beam is given as follows:

$$\kappa_g(x) = \frac{\frac{d^2y}{dx^2}}{\left[1+\left(\frac{dy}{dx}\right)^2\right]^{3/2}} = \frac{1}{R_o} - \frac{M(x)}{EI(x)} \tag{3}$$

where the Young's modulus, E, of nitinol is as provided by the manufacturer as approximately 40 GPa to 45 GPa (45 GPa was chosen for the large deflection model). The integral approach introduced in [22] is used to determine the governing equations for our beam:

$$\frac{ds}{dx} = \frac{1}{\sqrt{1-H^2(x)}} \tag{4}$$

$$\frac{dy}{dx} = \frac{H(x)}{\sqrt{1-H^2(x)}} \tag{5}$$

where $H\left(x\right) = \int_0^x \left(\frac{1}{R_o} - \frac{M(x)}{EI(x)}\right)dx$. This is a variant of the method proposed in [22] for curved beams with path-varying cross-sections and loads. For a given projected final length of the curved beam (onto the x-axis), l, the total length of the beam can be determined by integrating Eq. (4) (see Fig. 3). By searching the projected length, l, until $|s(l) - L| < \varepsilon_{err}$, we arrive at the final solution for the path of the beam under gravity loading. The search space and the computation time can be reduced from the monotonicity of $s(l)$ with respect to l [22], however, this approach only works for beam tip deflections under 90°. Here, ε_{err} is a normalized error margin. Once the final projected length, l, of the beam is known, Eq. (5)

can be solved to determine the final Cartesian coordinates of the beam. Since the distributed load and second moments of area ($w(s)$ and $I(s)$) are given as a function of arc-length, s, which is a function of loading w, we divide the load, ρg, into N_{load} equal steps [23]. At each load step, $j = 1,2,\ldots, N_{load}$, the path information of the previous load step (solution to Eq. (4)) and the current load are used to determine shear forces and bending moments:

$$V^j(x) = \int_x^l w^j\left(x^{j-1}\right)dx \tag{6}$$

$$M^j(x) = \int_x^l V^j(x)dx \tag{7}$$

The moment, thus approximated, is used to determine $H^j\left(x\right)$ in Eqs. (4–5). A similar procedure is used to approximate $I^j\left(x\right)$ (second moment of area of the current load step) from Eq. (4) and $I\left(s^{j-1}\right)$. These values are then used to determine the final projected length, l, and therefore, the shape of the beam for each load step, until the final N_{load} step. Section IV–A presents a validation of this approach in Finite Element models as well as experimental validation.

B. Combined Tube Curvatures

When the COAST mechanism is assembled completely, the final pre-curvature of its bending segment is determined by the pre-curvatures, moments and the flexural rigidity of the individual beams comprising the assembly, primarily the outer and middle tubes (see Fig. 4). We use a modified version of the method proposed in [24] to achieve the final curvature of the tube as follows:

$$\kappa_{final}(s) = \left[\sum_{k=1}^{N_t} E_k I_k(s)\right]^{-1}\left[\sum_{k=1}^{N_t} E_k I_k(s)\kappa_{g,k}(s)\right] \tag{8}$$

where $N_t = 2$ is the number of micromachined tubes in our mechanism and individual curvatures $\kappa_{g,k}(s)$ are obtained from Eqs. (3) and (4). Note, that unlike [24], gravity has a significant contribution to the final shape of the pre-curvature and leads to large deflections in the individual tubes (and is included in the term $\kappa_{g,k}(s)$. Finally, $\kappa_{final}(s)$ is a piecewise function of s, much like $\kappa_g(s)$, $I(s)$, and $w(s)$, due to varying cross-sections. Therefore, the total pre-curvature in any given telescoping combination of outer and middle tubes will be considered and is given by $\int_{s=0}^{L}|\kappa_{final}(s)|$.

The tubes are assembled as shown in Fig. 4, with the middle tube naturally curving in the direction of gravity. The outer tube is assembled coaxially over the middle tube and oriented 180° out of phase, hence naturally curving opposite to the direction of gravity. While the combined pre-curvature of the assembled pair would be affected by the choice of orientation of the tubes, we keep this choice consistent across all the pairs to evaluate the best sample. Section IV–B details the pair combinations tested experimentally and the pair combination

selected for the COAST robot construction. The modeling described in Sections III–A and III–B are used only for the purpose of design selection (notch depths, d_{mid} and d_{out}) and assembly of the COAST guidewire robot.

C. Bending Joint Model

A simplified schematic of the COAST guidewire is shown in Fig. 5, where the notched joint represents the bending segment (only middle tube shown) and a shortened tendon. The tendon stroke (X_1) required for a desired curvature (κ) over the bending segment, at a certain bending segment length (X_2), is derived as:

$$X_1 = \underbrace{\Delta L^{kin}(\kappa, X_2)}_{\text{Geometric term}} + \underbrace{\frac{\sigma_t L_{total}}{E_t}}_{\text{Tendon elongation}} \tag{9}$$

$$= \Delta L^{kin}(\kappa, X_2) + \frac{F_t L_{total}}{\pi E_t r_t^2} \tag{10}$$

The expression for the geometric term, $\Delta L^{kin}(\kappa, X_2)$, in the above model equation is derived in [13] (omitted here for brevity). Tendon elongation is, however, the dominant term in this relationship, and it depends on the stress in the tendon, given by $\sigma_t = F_t/(\pi r_t^2)$. Here, F_t is the tendon tension at the actuator (see Fig. 5), $r_t = 38\mu$m is the tendon radius, and $L_{total} = 388.68$ mm is the undeformed total tendon length (from attachment point on the actuator to the guidewire tip).

We assume that primarily, friction losses occur from the pulleys in the CAS and tendon-notch interactions. Accounting for these losses as in [25], [26], the tendon tension can be expressed in terms of the bending moment applied to the joint tip as:

$$F_t = e^{\mu\alpha}\eta^{N_f}\frac{M_t}{\Delta y_t} \tag{11}$$

where M_t is the applied moment by the tendon, Δy_t is the moment arm of the tendon at the distal end of the robot, μ is the coefficient of friction of the pulleys in the CAS, while η is the friction loss occurring due to cable interactions with the notch edges (such that $F_2 = \eta F_1$ in Fig. 5(inset)). The total number of notches in contact with the tendon is estimated as $N_f = (X_2 N_{mid})/L_{mid}^{notch}$ (N_{mid} and L_{mid}^{notch} being the number of notches and the length of the notched section for the middle tube, respectively).

Substituting Eq. (11) in Eq. (10), and relating applied tension, F_t, to the curvature, κ, (using the Euler beam model proposed in [13]) the joint kinematics model is completed as follows:

$$X_1 = \Delta L^{kin}(\kappa, X_2) + e^{\mu\alpha}\eta^{N_f}\frac{E(I_{out} + I_{mid})L_{total}}{\Delta y_t E_t \pi r_t^2}\kappa \tag{12}$$

where E is the elastic modulus of the tubes, and I_{mid} and I_{out} are the second moments of area of the middle and outer tubes, respectively. The model is validated by observing the

experimental data between tendon stroke, X_1, and bending curvature, κ, keeping bending length, X_2, as constant.

IV. Validation of Mechanical Models

A. Curved Beam Bending Model Results

First, we validated our large-deflection curved beam model with finite element simulations in ANSYS® 18.2 for stainless steel ($E = 200$GPa) beams with a single long notch ($N = 1$). The numerical integration for $H(x)$, Eq. (4), and $s(l)$ for various values of l at each load step were computed on a 20 core Intel® Xeon® Processor using the parallel processing toolbox in MATLAB® R2020b. The tube dimensions (r_o, r_i, d, R_o, and L) were varied to match the outer and middle tubes. In each case, we observe that the numerical model (Eq. (5)) accurately predicts the final shape of the curved beam for both positive and negative initial curvatures (see Fig. 6). We then proceed to test our model experimentally for outer and middle tubes sampled with varying notch parameters (see Fig. 7). To obtain the shape of the notched nitinol tubes deformed under gravity from the images using the CMOS camera, we first perform adaptive thresholding to get a binarized image of the tubes. We then apply the multivariate adaptive regression spline (MARS) algorithm [27] to compute a a smooth spline representing the shape of the deformed tube using the ARESLab toolbox [28] such as in our previous work [29].

To quantify the error between the FEM simulation and the model arcs (Fig. 6(a)–(d)) the RMSE value between the two lines is then calculated where the error at each point is the Euclidean distance between each coordinate pair on the FEM and model arcs corresponding to the same arc lengths. If the number of nodes between the FEM model and the proposed model differed, the values were linearly interpolated to match the position along the arc length. The RMSE values for the plots shown in Fig. 6 are given in Table III.

Similarly, the RMSE values for the plots shown in Fig. 7 are calculated and are shown in Table III. It is observed that as the MARS algorithm fits an optimized spline based on the area of the binarized image of the deformed tube, which is influenced by the presence of notches, which contributes to the error between the model and the experimental deformation data. We observe that the model successfully estimates the shape of the beams for all middle tube samples and all outer tube samples with positive curvatures (see Fig. 7(a)–(c)). The model begins to deviate from the experimental results for outer tubes with negative pre-curvatures (see Fig. 7(d) and Table III). It is hypothesized that this may be due to the machining tolerances that especially affect higher deformations of initially pre-curved notched beams when the pre-curvatures are in the direction of the distributed force (gravity).

B. Combined Tube Curvature Model Results

Fig. 8(a)–(b) are plots of 12 samples (S1, S2, …, S12) of coaxially combined middle and outer tube pairs. The plot in Fig. 8(a) displays the ratios of the flexural rigidity of the outer-tube to that of the middle tube $\left(\int_{s=0}^{L} I_{out}(s) / \int_{s=0}^{L} I_{mid}(s)\right)$ vs. the total pre-curvature $\left(\int_{s=0}^{L} |\kappa_{final}(s)|\right)$ for each sample. Furthermore, Fig. 8(b) represents a graph of flexural rigidity of the samples $\left(\int_{s=0}^{L} I_{out}(s) + I_{mid}(s)\right)$ vs. the total pre-curvature in the samples. The shaded

lines are shown in Fig. 8(a) to indicate the total curvature vs. ratio of rigidity trends when varying outer tube notch depths (d_{out}) and keeping the middle tube notch depth as constant (d_{mid}). We observe that sample S1 has the lowest predicted pre-curvature, but suffers from relatively higher dominance of the outer tube's rigidity in comparison to sample S4, which demonstrates lowest rigidity ratio (see Fig. 8(a)). In fact, sample S1 demonstrates the highest total flexural rigidity and hence may be unsuitable for a guidewire application due to the risk of vascular perforation (see Fig. 8(b)) upon tip contact with the vessel walls.

When assembling the notched middle and outer tubes, low total combined curvature of the tube pair is desired to achieve a straight initial configuration of the robot (as mentioned in Section III). Low total flexural rigidity is desired to allow for ease of actuating the bending joint, and preventing excessive trauma due to vascular collisions. The ratio of flexural rigidities for the tube pair is desired to be close to unity so that the rigidity of the one tube does not dominate the other, which further leads to a non-zero combined curvature. For moderate to high total combined curvatures of the tube pairs, such that the robot curved in the direction of the outer tube (when its rigidity was dominant), an initial snapping motion was observed upon actuating the tendon stroke to a certain value as the curvature of the robot switched to being dictated by the actuated middle tube's bending length. This effect was further observed in the experimental trials performed to validate the bending joint model described in Section III–C. To achieve the requirements of the parameters as described above, we therefore selected sample S4 ($d_{mid} = 0.243\,\text{mm}$ and $d_{out} = 0.400\,\text{mm}$) as our best sample with the combination of relatively low rigidity, minimal pre-curvature, and ratio of flexural rigidity closest to unity, resulting in no observed snapping motion.

C. Bending Joint Model Results

We validated the joint kinematics model for different pairs of outer and inner tubes with bending lengths varying as $X_2 = \{20,25,30,35,40\}\text{mm}$. A CMOS camera is used to image the deflection of the bending section by setting the imaging plane parallel to the plane of bending. The curvature (κ) of the bending segment is extracted from the acquired images and plotted against the tendon stroke (X_1), for different values of the bending segment length (X_2), as shown in Fig. 9(a) for the tube pair S4 selected from Section III–B. We observe a hysteretic lag in the motion of the bending joint when releasing the tendon i.e., decreasing the tendon stroke (X_1). The model described by Eq. (12) is hence validated only for the motion in the direction of actuation i.e., increasing tendon stroke. Furthermore, an initial pre-tensioning and elongation of the tendon does not result in actuation of the bending segment, resulting in no curvature being detected by the camera. This pre-tension deadband stroke length is experimentally determined to be 1.2 mm. The tendon stroke range for all plots in Fig. 9(a)–(c) are offset by this deadband value. The model is observed to be in agreement with the experimental results. We observe some initial deviation for the bending lengths $X_2 > 25\,\text{mm}$. This non-linearity is attributed to the high compliance of the outer tube as a result of high notch depth. Fig. 9(b) also shows the variation of the $X_1 - \kappa$ relation when the notch depths for only the outer tube are varied. Similarly Fig. 9(c) shows the $X_1 - \kappa$ relation when the notch depths for only the middle tube are varied. Eq. (12), hence, also models the variation of notch depth for the individual tubes as seen in these figures.

Deviations from the model, as seen for lines corresponding to $d_{out} = 0.376\,\text{mm}$ (red) and $d_{out} = 0.314\,\text{mm}$ (blue) in Fig. 9(b) are mainly attributed to machining inaccuracies. While laser parameters were kept constant across all samples, some variations in positioning of the tubes to be machined were necessary (e.g., focusing height of the laser, number of repetitions of the pattern etc.). The coefficients of friction were estimated by manually calibrating the model to fit the data for sample S4 (Fig. 9(a)), and were estimated to be $\mu = 0.2965$ and $\eta = 1.0063$. Additionally, the value for the elastic modulus of the nitinol tubes was also varied (within the manufacturer specified range of 40~45GPa to obtain a final estimate of $E = 42.6\text{GPa}$. Deviation from the elastic modulus' original value can be attributed to the heating effects when machining the notches on the tubes with the femtosecond laser, as mentioned in Sections II–A and III. Minor variations in the friction coefficients can be attributed to the machining process as well (burrs at the notch edges), which may be tuned further for the selected prototype to obtain a better fitting model. This calibration process to obtain the values of E, μ, and η was further used in our previous work to demonstrate and analyze the bending and navigational accuracy of the COAST robot [30]. The RMSE values for the curvature errors are shown in Table IV and the RMSE values for the final tip position errors due to the error in the curvature are shown in Table V. The average of the RMSE values of the COAST guidewire robot tip position error for the validation study, corresponding to Fig. 9(b) and Fig. 9(c) as shown in Table V, was calculated to be 0.816 mm. The model, with the calibrated E, μ, and η values can now be used to estimate the bending behavior as well as choose the required notch parameters $\{d, c, h\}$ for machining.

V. Conclusions

In this work, a design procedure for the COaxially Aligned STeerable (COAST) guidewire robot was developed to select the appropriate machining parameters for the outer and middle nitinol tubes. A modified integral approach for nonuniform curved beams with large deflections was proposed and validated to estimate the pre-curvatures in the individual micromachined tubes of the COAST robot. Using these individual tube pre-curvatures and a combined deformation model for the telescoping micromachined tubes, the total precurvature in the COAST distal tip can be estimated. Then, the geometric properties of micromachining can be adjusted for high compliance and low pre-curvatures. Finally, a modified joint kinematics and statics model was formulated by considering friction within the bending joint and the CAS. The model was validated for all tube pairs and was shown to predict the tendon stroke for the required curvature values. Future works will account for the presence of external forces on the robot, such as contact with vascular walls and blood flow, and use improved modeling approaches for control under flouroscopic guidance.

Acknowledgments

Research reported in this publication was supported in part by the National Heart, Lung, And Blood Institute of the National Institutes of Health under Award Number R01HL144714. The content is solely the responsibility of the authors and does not necessarily represent the official views of the National Institutes of Health.

References

[1]. Roth GA, Abate D, Abate KH, Abay SM, Abbafati C, Abbasi N, Abbastabar H, Abd-Allah F, Abdela J, Abdelalim A, et al. , "Global, regional, and national age-sex-specific mortality for 282 causes of death in 195 countries and territories, 1980–2017: a systematic analysis for the global burden of disease study 2017," The Lancet, vol. 392, no. 10159, pp. 1736–1788, 2018.

[2]. Vos T, Allen C, Arora M, Barber RM, Bhutta ZA, Brown A, Carter A, Casey DC, Charlson FJ, Chen AZ, et al. , "Global, regional, and national incidence, prevalence, and years lived with disability for 310 diseases and injuries, 1990–2015: a systematic analysis for the global burden of disease study 2015," The Lancet, vol. 388, no. 10053, pp. 1545–1602, 2016.

[3]. Benjamin EJ, Virani SS, Callaway CW, Chamberlain AM, Chang AR, Cheng S, Chiuve SE, Cushman M, Delling FN, Deo R, et al. , "Heart disease and stroke statistics-2018 update: a report from the american heart association." Circulation, vol. 137, no. 12, pp. 67–492, 2018.

[4]. Kim Y, Parada GA, Liu S, and Zhao X, "Ferromagnetic soft continuum robots," Science Robotics, vol. 4, no. 33, p. eaax7329, 2019.

[5]. Kim J, Nguyen PB, Kang B, Choi E, Park J-O, and Kim C-S, "A novel tip-positioning control of a magnetically steerable guidewire in sharply curved blood vessel for percutaneous coronary intervention," International Journal of Control, Automation and Systems, vol. 17, no. 8, pp. 2069–2082, 2019.

[6]. Yun C-H, Yeo LY, Friend JR, and Yan B, "Multi-degree-offreedom ultrasonic micromotor for guidewire and catheter navigation: The neuroglide actuator," Applied Physics Letters, vol. 100, no. 16, p. 164101, 2012.

[7]. Sheng J, Wang X, Dickfeld T-ML, and Desai JP, "Towards the development of a steerable and MRI-compatible cardiac catheter for atrial fibrillation treatment," IEEE Robotics and Automation Letters, vol. 3, no. 4, pp. 4038–4045, 2018. [PubMed: 30923746]

[8]. Ali A, Plettenburg DH, and Breedveld P, "Steerable catheters in cardiology: Classifying steerability and assessing future challenges," IEEE Transactions on Biomedical Engineering, vol. 63, no. 4, pp. 679–693, 2016. [PubMed: 26863645]

[9]. Webster RJ, Romano JM, and Cowan NJ, "Mechanics of precurved-tube continuum robots," IEEE Transactions on Robotics, vol. 25, no. 1, pp. 67–78, 2009.

[10]. Deaton NJ, Brumfiel TA, Sarma A, and Desai JP, "Simultaneous shape and tip force sensing for the coast guidewire robot," IEEE Robotics and Automation Letters, vol. 8, no. 6, pp. 3725–3731, 2023.

[11]. Chitalia Y, Wang X, and Desai JP, "Design, modeling and control of a 2-dof robotic guidewire," in 2018 IEEE International Conference on Robotics and Automation (ICRA). IEEE, 2018, pp. 32–37.

[12]. Soyama T, Yoshida D, Sakuhara Y, Morita R, Abo D, and Kudo K, "The steerable microcatheter: a new device for selective catheterisation," Cardiovascular and Interventional Radiology, vol. 40, no. 6, pp. 947–952, 2017. [PubMed: 28138724]

[13]. Jeong S, Chitalia Y, and Desai JP, "Design, modeling, and control of a coaxially aligned steerable (COAST) guidewire robot," IEEE Robotics and Automation Letters, vol. 5, no. 3, pp. 4947–4954, 2020.

[14]. Chitalia Yash Chetan, "Design, Modeling and Control of Micro-scale and Meso-scale Tendon-Driven Surgical Robots," Ph.D. dissertation, Georgia Institute of Technology, 2021.

[15]. Barrientos-Diez J, Russo M, Dong X, Axinte D, and Kell J, "Asymmetric continuum robots," IEEE Robotics and Automation Letters, vol. 8, no. 3, pp. 1279–1286, 2023.

[16]. Anor T, Madsen JR, and Dupont P, "Algorithms for design of continuum robots using the concentric tubes approach: A neurosurgical example," in 2011 IEEE International Conference on Robotics and Automation, 2011, pp. 667–673. [PubMed: 22270831]

[17]. Clogenson HCM and Simonetto A and J.J. van den Dobbelsteen, "Design optimization of a deflectable guidewire," Medical Engineering Physics, vol. 37, no. 1, pp. 138–144, 2015. [PubMed: 25455166]

[18]. Ros-Freixedes L, Gao A, Liu N, Shen M, and Yang G-Z, "Design optimization of a contact-aided continuum robot for endobronchial interventions based on anatomical constraints," International

journal of computer assisted radiology and surgery, vol. 14, pp. 1137–1146, 2019. [PubMed: 30989504]

[19]. Chitalia Y, Wang X, Nguyen V, Melkote S, Chern J, and Desai JP, "Design and analysis of a bidirectional notch joint for a robotic pediatric neuroendoscope," in International Symposium on Experimental Robotics. Springer, 2018, pp. 24–33.

[20]. Chitalia Y, Jeong S, Yamamoto K, Chern JJ, and Desai JP, "Modeling and control of a 2-dof meso-scale continuum robotic tool for pediatric neurosurgery," IEEE Transactions on Robotics, 2020.

[21]. Bargeron CB, Hutchins GM, Moore GW, Deters OJ, Mark FF, and Friedman MH, "Distribution of the geometric parameters of human aortic bifurcations." Arteriosclerosis: An Official Journal of the American Heart Association, Inc., vol. 6, no. 1, pp. 109–113, 1986. [Online]. Available: https://www.ahajournals.org/doi/abs/10.1161/01.ATV.6.1.109 [PubMed: 3942554]

[22]. Chen L, "An integral approach for large deflection cantilever beams," International Journal of Non-Linear Mechanics, vol. 45, no. 3, pp. 301–305,2010.

[23]. Ghuku S and Saha KN, "A theoretical and experimental study on geometric nonlinearity of initially curved cantilever beams," Engineering Science and Technology, an International Journal, vol. 19, no. 1, pp. 135–146, 2016.

[24]. Dupont PE, Lock J, Itkowitz B, and Butler E, "Design and control of concentric-tube robots," IEEE Transactions on Robotics, vol. 26, no. 2, pp. 209–225, 2009.

[25]. Cheng SS, Wang X, and Desai JP, "Design and analysis of a remotely-actuated cable-driven neurosurgical robot," in 2017 IEEE/RSJ International Conference on Intelligent Robots and Systems (IROS). IEEE, 2017, pp. 1685–1690.

[26]. York PA, Swaney PJ, Gilbert HB, and Webster RJ, "A wrist for needle-sized surgical robots," in Robotics and Automation (ICRA), 2015 IEEE International Conference on. IEEE, 2015, pp. 1776–1781.

[27]. Friedman JH, "Multivariate adaptive regression splines," The Annals of Statistics, pp. 1–67, 1991.

[28]. Jekabsons G, "ARESLab: Adaptive regression splines toolbox for Matlab/Octavehttp," 2011.

[29]. Deaton NJ, Sheft M, and Desai JP, "Towards fbg-based shape sensing and sensor drift for a steerable needle," IEEE/ASME Transactions on Mechatronics, 2023, (accepted).

[30]. Sarma Achraj and Brumfiel Timothy A. and Chitalia Yash and Desai Jaydev P., "Kinematic Modeling and Jacobian-Based Control of the COAST Guidewire Robot," IEEE Transactions on Medical Robotics and Bionics, vol. 4, no. 4, pp. 967–975, 2022.

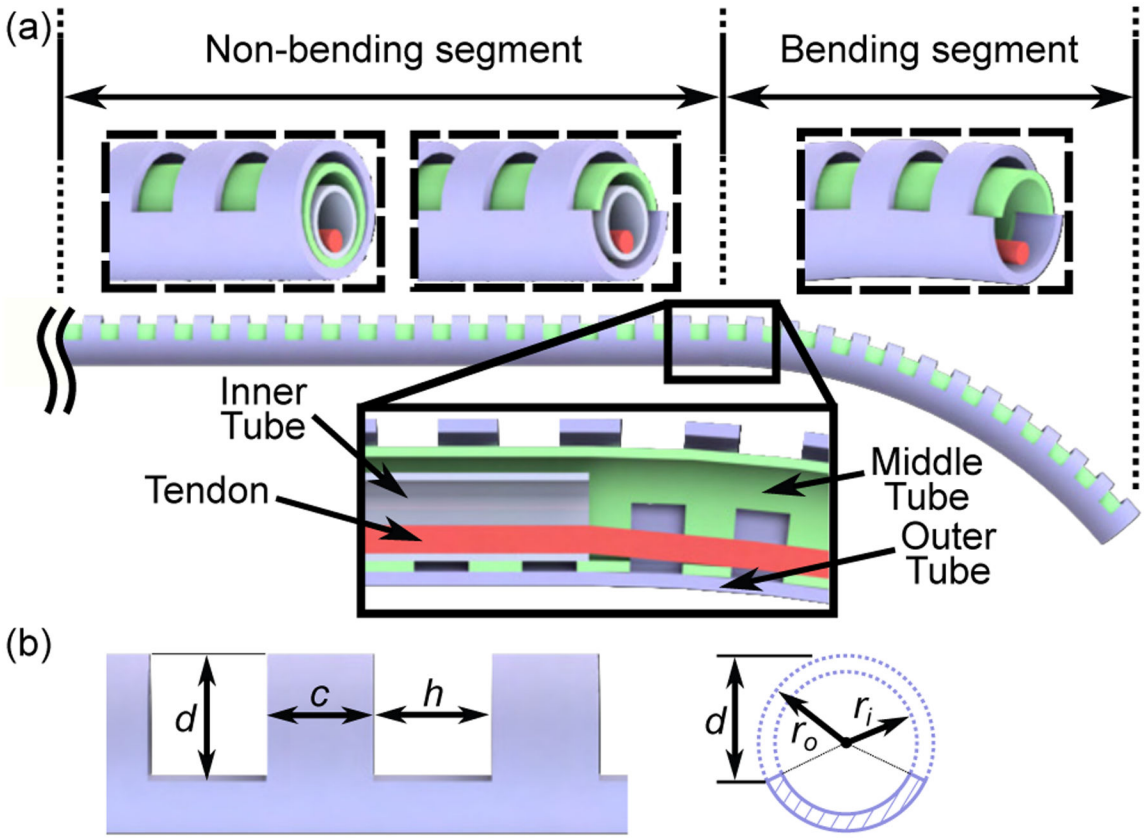

Fig. 1:

(a) Internal structure of the COAST guidewire with two micromachined nitinol tubes, a stainless-steel inner tube, and a single nitinol tendon, (b) Illustration of notch parameters on the micromachined nitinol tubes.

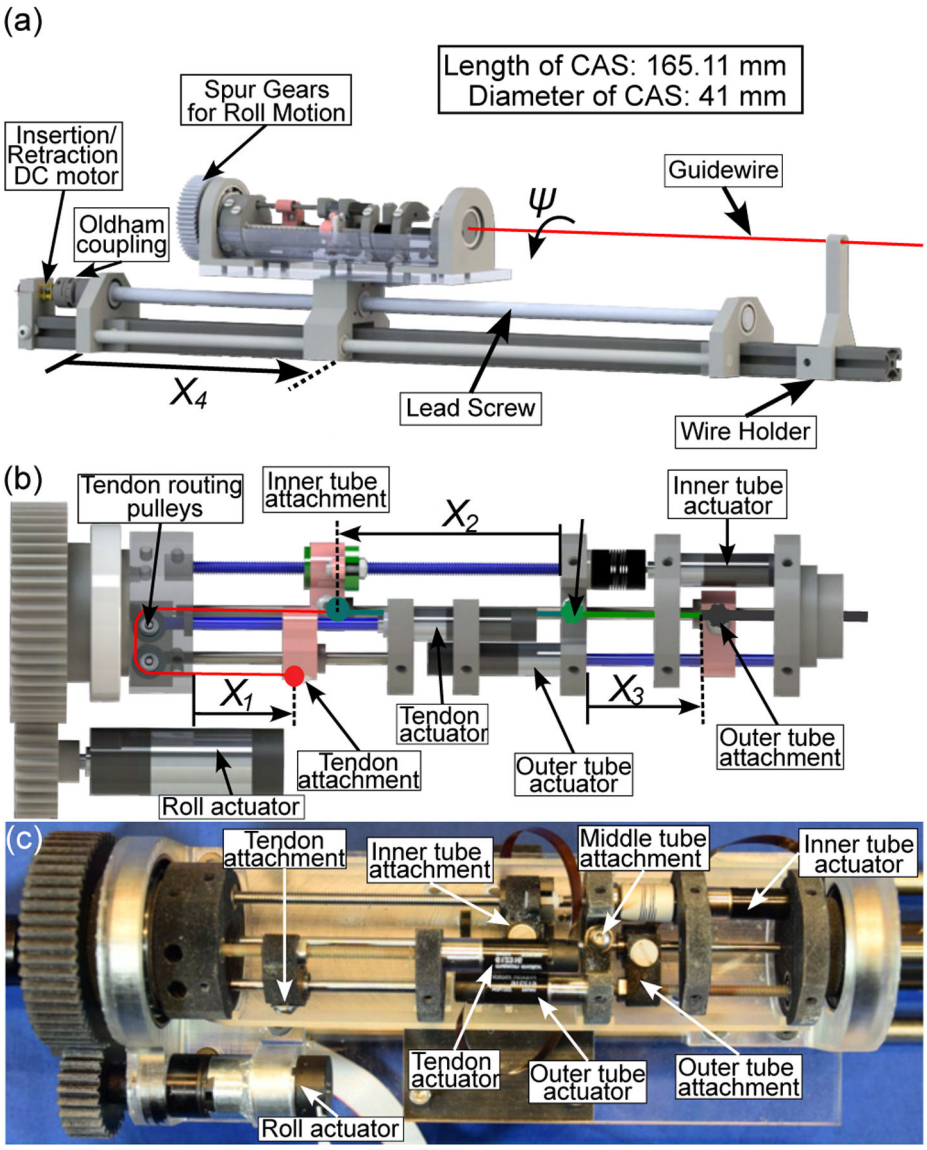

Fig. 2:

(a) Schematic of the CAS for the COAST guidewire. The driving unit shows the DC motor and lead screw assembly that enables the entire setup to be compact, (b) Inner mechanism of the CAS and control variables for individual tubes (adapted from [14]), (c) Image of inner mechanism (adapted from [14]).

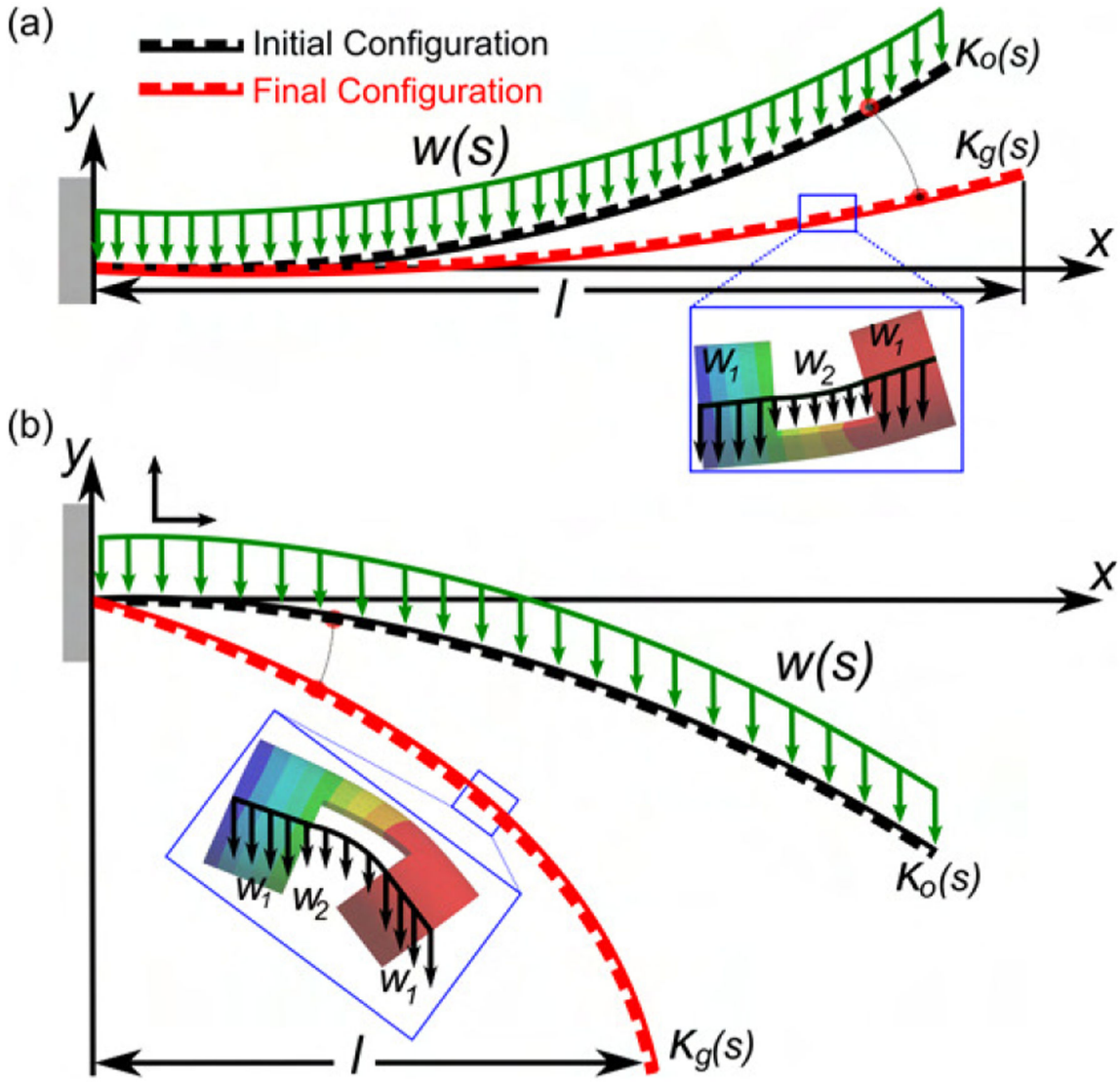

Fig. 3:
Curved micromachined beam with gravity induced large deflections for (a) positive and (b) negative initial curvatures.

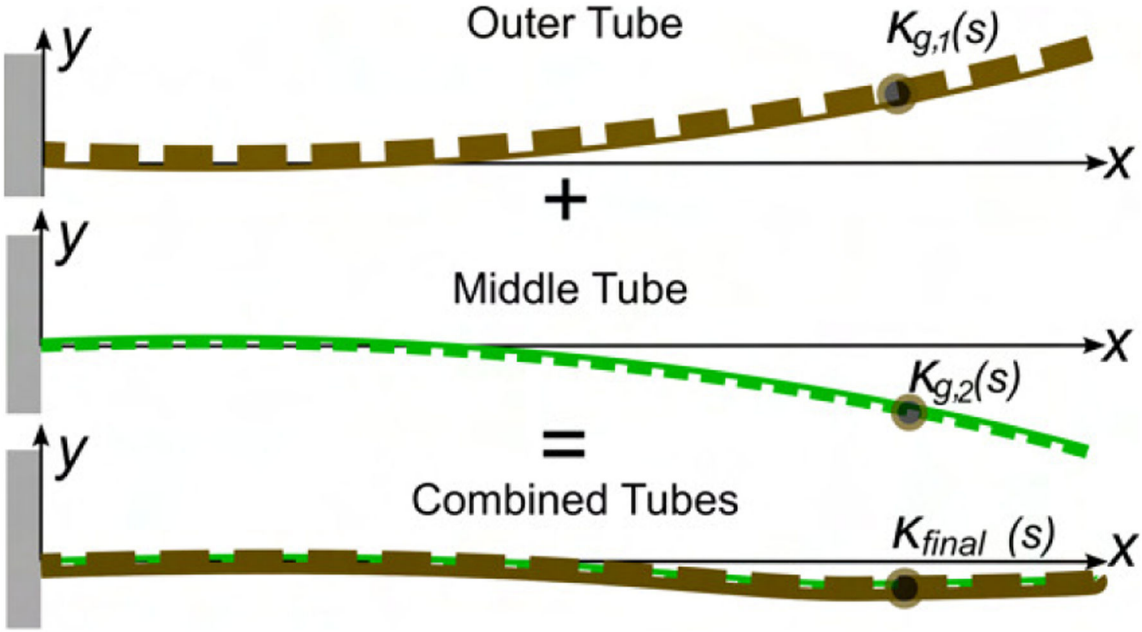

Fig. 4:
Combined beam bending behavior of the outer and middle tubes (adapted from [14]).

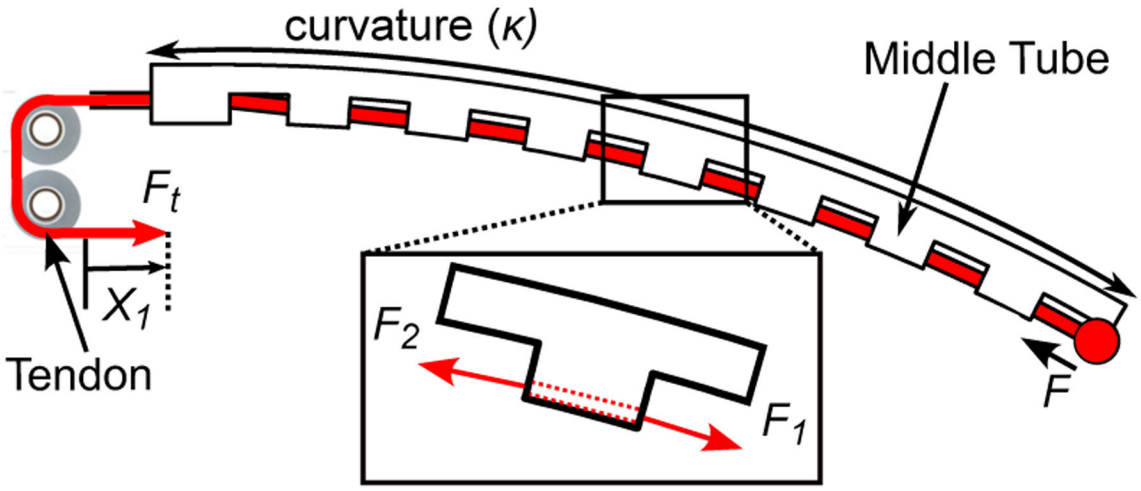

Fig. 5:
Schematic of guidewire bending segment showing forces at the tip (F), and the actuator (F_t) (adapted from [14]).

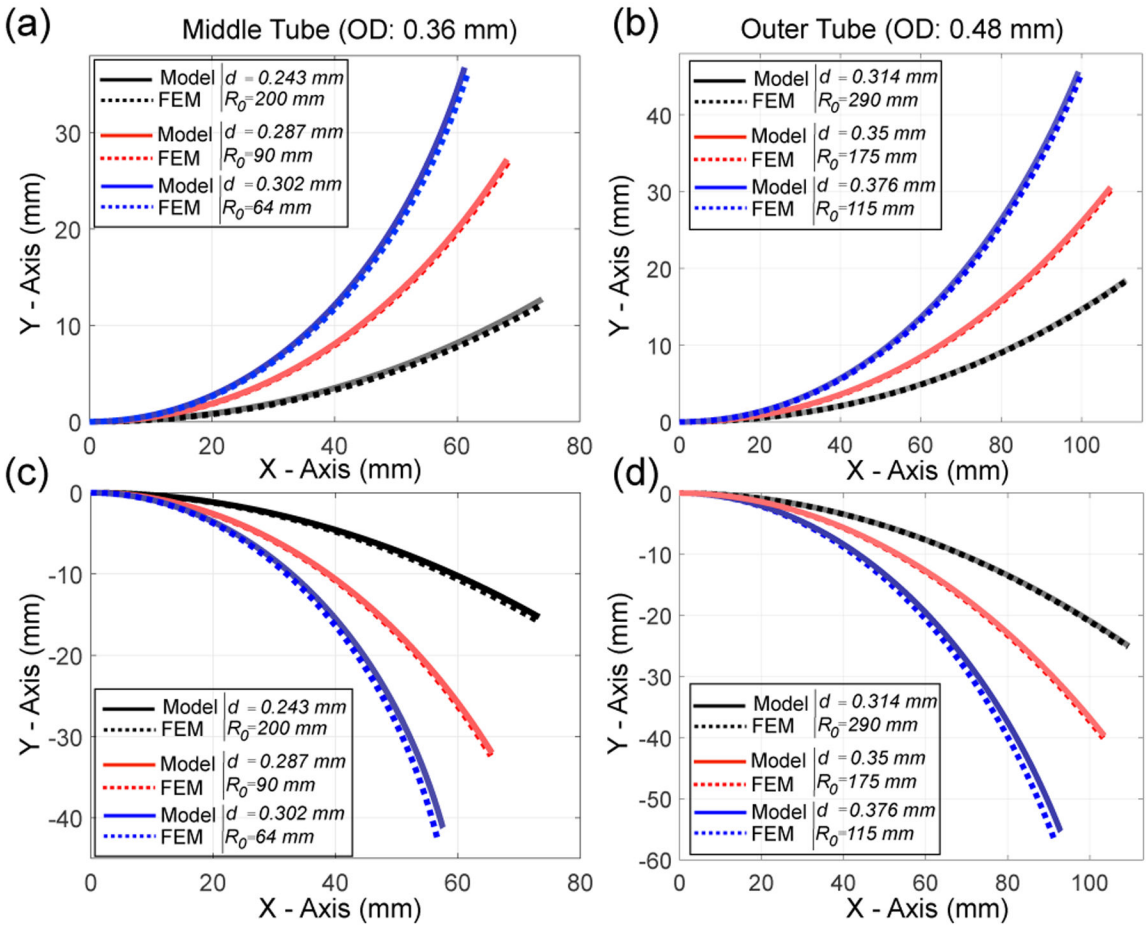

Fig. 6:

Validation of the curved beam bending model in ANSYS for (a)-(b) positive pre-curvatures and (c)-(d) negative pre-curvatures for stainless steel tubes with $N = 1$ and varying r_o, d, and R_o values (adapted from [14])

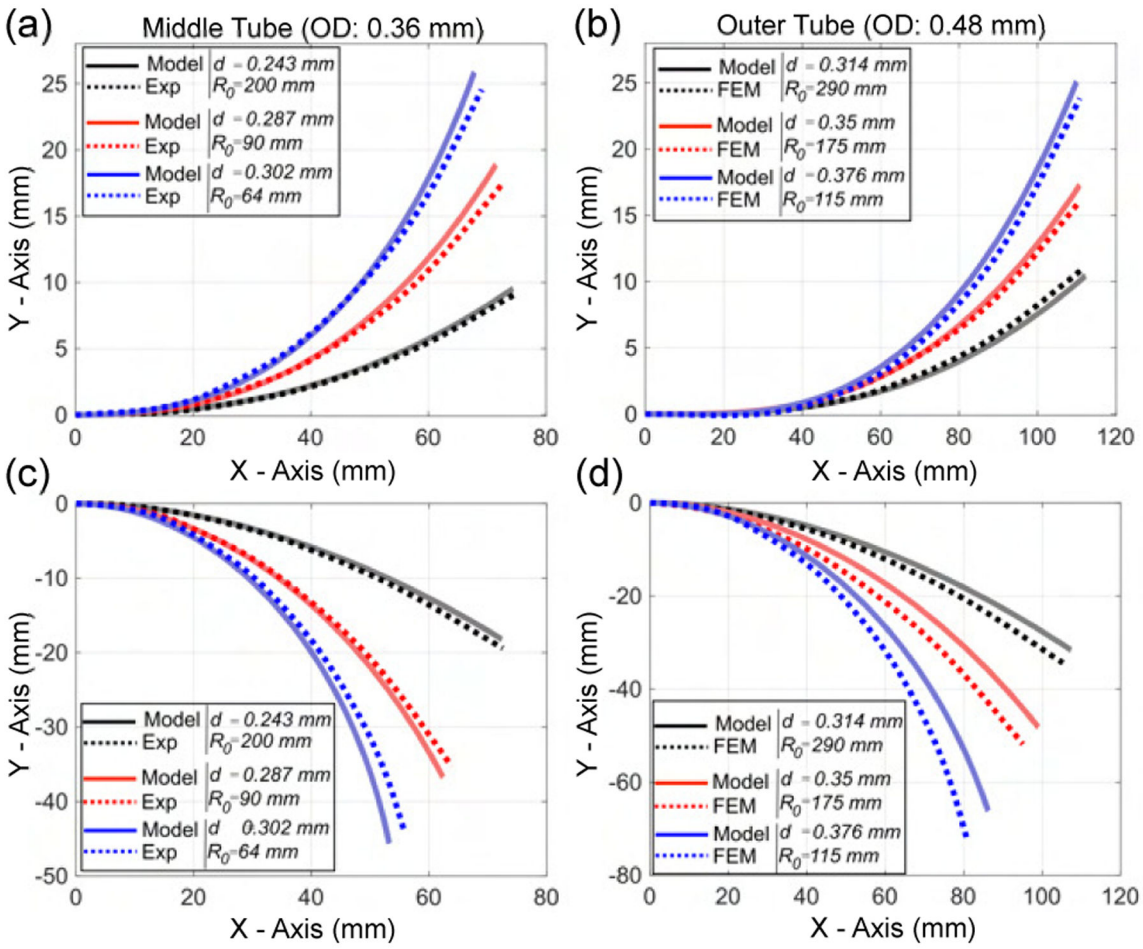

Fig. 7:

Validation of the curved beam bending model for experimental data with (a)-(b) positive pre-curvatures and (c)-(d) negative pre-curvatures for tubes with varying $N = \{125,188\}, r_o, d$, and R_o values (adapted from [14]).

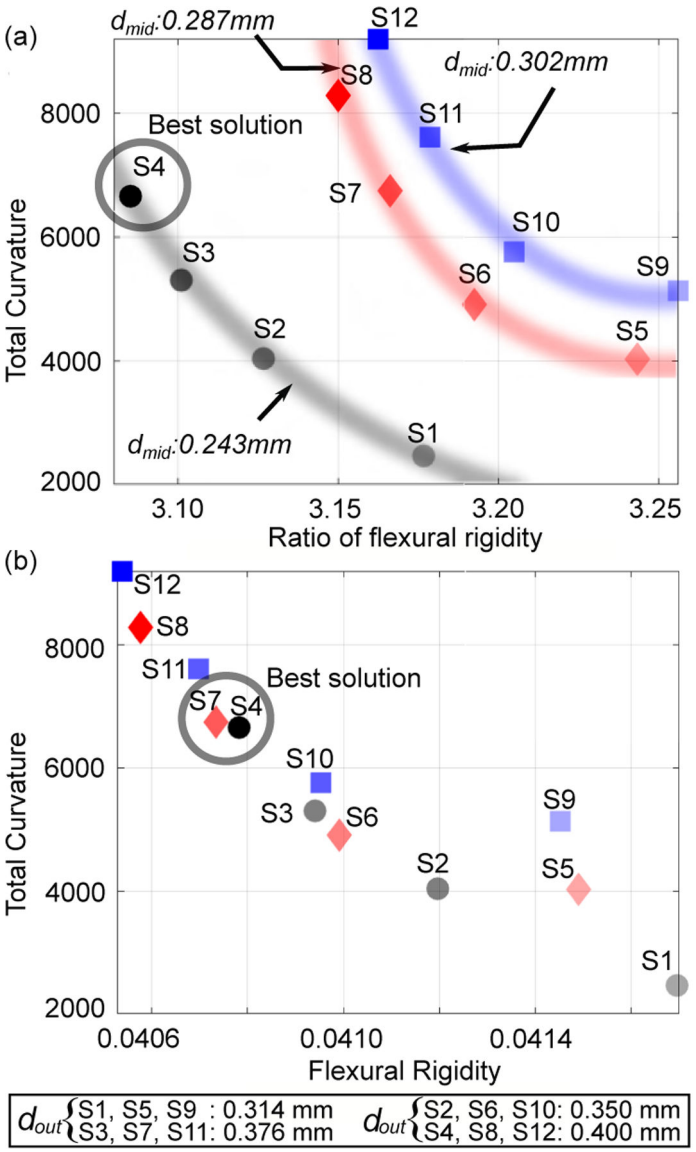

Fig. 8:

(a) Graph of flexural rigidity ratios of the outer to the middle tube vs. total curvature in the combined tube samples. (The shaded lines are shown to indicate the trends when varying d_{out} and keeping d_{mid} as constant), (b) Graph of flexural rigidity vs. total combined curvature. Depths of the middle and outer tubes are given by d_{mid} and d_{out} respectively (adapted from [14]).

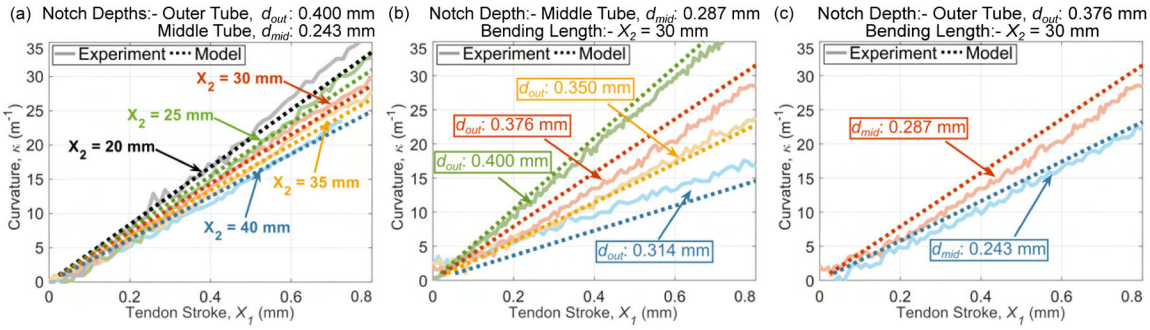

Fig. 9:

Plots showing variation of curvature (κ) vs. tendon stroke (X_1) in joint loading case: (a) varying bending lengths (X_2) for sample S4, (b) varying outer tube's notch depths for constant middle tube and bending length, and (c) varying middle tube's notch depths for constant outer tube and bending length. Solid and dashed lines indicate experimental and modeled data, respectively (adapted from [14]).

TABLE I:

Specifications of the COAST guidewire prototype.

Items	Outer tube	Middle tube	Inner tube	Tendon
Total length (mm)	242.00	253.10	269.50	388.68
Length of the notched section (mm)	112.8	75.0	-	-
Outer diameter, $2r_o$, (mm)	0.480	0.360	0.254	0.076
Inner diameter, $2r_i$, (mm)	0.400	0.300	0.239	-
Notch depth, d (mm)	0.400	0.243	-	-
Notch spacing, c (mm)	0.285	0.285	-	-
Notch width, h (mm)	0.315	0.315	-	-
Young's modulus (GPa)	40~45	40~45	200	53.965

TABLE II:

Notch depths of micromachined outer and middle nitinol tubes.

Tube	OD (mm)	Notch Depth, d, (mm)			
		$d_{out,1}$	$d_{out,2}$	$d_{out,3}$	$d_{out,4}$
Outer Tube	0.480	0.314	0.350	0.376	0.400
		$d_{mid,1}$	$d_{mid,2}$	$d_{mid,3}$	
Middle Tube	0.360	0.243	0.287	0.302	

TABLE III:

RMSE values for FEM (Fig. 6)/experimental(Fig. 7) and curved beam bending model deflection values for varying middle tube notch depths (d_{mid}) and outer tube notch depths (d_{out}). Lengths of notched section considered for middle tube, $L_{mid}^{notch} = 75\,\text{mm}$ and for outer tube, $L_{mid}^{notch} = 112.8\,\text{mm}$.

Fig.	RMSE (mm)			Fig.	RMSE (mm)		
d_{min}:(mm)	0.243	0.287	0.302	d_{out}:(mm)	0.314	0.350	0.376
6(a)	0.264	0.160	0.394	**6(b)**	0.064	0.171	0.417
6(c)	0.263	0.185	0.736	**6(d)**	0.077	0.219	1.094
7(a)	0.168	0.569	0.531	**7(b)**	0.329	0.334	0.640
7(c)	0.540	0.673	1.154	**7(d)**	1.755	3.202	3.160

TABLE IV:

RMSE values (in m^{-1} for experimental and modeled curvature (κ) vs. tendon stroke data (X_1) for varying bending lengths (X_2), outer tube notch depths (d_{out}), and middle tube notch depths (d_{mid}) (Fig. 9).

Fig.		**RMSE (m^{-1})**				
	X_2 (mm):-	20	25	30	35	40
9(a)		1.605	1.405	0.833	0.883	0.748
	d_{out} (mm):-	0.314	0.350	0.376	0.400	
9(b)		2.457	0.921	2.306	1.520	
	d_{mid} (mm):-	0.243	0.287			
9(c)		1.164	2.306			

TABLE V:

RMSE values (in mm) of COAST robot tip position errors corresponding to the bending joint model results (Fig. 9).

Fig.		Tip Position Error (mm)				
	X_2 (mm):-	20	25	30	35	40
9(a)		0.304	0.430	0.366	0.537	0.600
	d_{out} (mm):-	0.314	0.350	0.376	0.400	
9(b)		1.104	0.395	1.024	0.662	
	d_{mid} (mm):-	0.243	0.287			
9(c)		0.422	1.287			